PHYSICAL REVIEW B **73**, 020402(R) (2006)

# Magnetotransport of magnetite nanoparticle arrays

Hao Zeng,[1,2] C. T. Black,[1] R. L. Sandstrom,[1] P. M. Rice,[3] C. B. Murray,[1] and Shouheng Sun[1,4]
[1]*IBM Thomas J. Watson Research Center, Yorktown Heights, New York 10598, USA*
[2]*Department of Physics, University at Buffalo, State University of New York, Buffalo, New York 14260, USA*
[3]*IBM Almaden Research Center, San Jose, California 95120, USA*
[4]*Department of Chemistry, Brown University, Providence, Rhode Island 02912, USA*
(Received 25 September 2005; published 3 January 2006)

We combine a material self-assembly with conventional lithographic processes in order to fabricate magnetoelectronic devices composed of ordered three-dimensional arrays of magnetite ($Fe_3O_4$) nanoparticles. The device magnetoresistance reaches 35% at 60 K, corresponding to an electron spin polarization of 73%. Magnetoresistance of 12% remains at room temperature. Magnetoresistance decreases with both increasing temperature and bias voltage, however, the magnetoresistance of nanoparticle-based structures is only weakly dependent on the voltage—a favorable attribute for application to electronics.

DOI: 10.1103/PhysRevB.73.020402 PACS number(s): 75.47.−m, 75.75.+a, 73.63.Bd

The rich scientific field of spin-dependent electronic transport has recently garnered additional attention because of its technological relevance to magnetic recording head sensors and its potential future application to magnetic random access memory and electronic logic devices.[1,2] One particularly interesting material for all of these future technologies is called a half-metal, which is characterized by the presence of an energy gap at the Fermi level ($E_F$) for only one electron spin direction (while the energy band for the opposite spin direction is continuous at $E_F$).[3] A complete spin polarization in materials with parallel and/or antiparallel magnetic moment orientations with and without fields would, in principle, give a magnetoresistance (MR) of 100% (50% in materials with randomly oriented magnetic moment directions in the absence of a field). Although magnetite ($Fe_3O_4$) has been predicted to be half-metallic, the reported MR values of single- and polycrystalline thin films and compacted powders[4–8] range from a few percent to 24% (Ref. 7) [$\mathrm{MR} \equiv (R-R_0)/R_0 \equiv \Delta R/R_0$, where $R_0$ is the zero-field resistance], which are generally smaller than what is expected for a half-metal. This is consistent with recent studies that suggest that complete spin polarization cannot be realized at finite temperatures.[9] Still, half-metals are promising candidates because their higher spin polarizations may beget larger magnetoresistance values at room temperature than more conventional ferromagnets.[10]

Granular magnetic materials—that is, systems comprised of large numbers of conducting islands in weak electrical contacts—can display enhanced spin-dependent electronic transport due to the high density of magnetic interfaces. For example, granular cobalt (Co) nanobridges show increased MR just above the Coulomb blockade threshold voltage.[11] Theoretical calculations and experimental results also suggest that the multiple junctions of granular materials decrease the material sensitivity to a bias voltage.[12,13] The difficulties of controlling grain size and spacing in granular materials have limited their use in technological applications.

Self-assembled nanoparticle arrays represent an idealized granular magnetic material, in that the nanoparticle size, spacing, and density can be controlled with high precision. Previous electrical measurements of conventional ferromagnet (Co) devices have yielded MR values consistent with expected material spin polarizations.[13] More recently, macroscopic films of $Fe_3O_4$ nanocrystals self-assembled by a Langmuir-Blodgett technique have shown very promising MR values (up to 300%).[14] In this work we have integrated magnetite nanoparticle arrays with conventional semiconductor microfabrication to produce multilayer devices, with the goal of exploring the electronic properties of such structures for potential applications.

Our fabrication process combines the utility of conventional microfabrication with the nanometer-scale precision of the nanoparticle self-assembly to produce devices with benefits from both techniques. We first sputter the device Pt counter electrode (200 nm) onto a $SiO_2$ substrate, followed by the chemical-vapor deposition of a $SiO_2$ dielectric (300 nm). We next use photolithography and plasma etching to create contact holes of different sizes in the $SiO_2$ dielectric—the dimensions of these contact holes determine the device active area. For the measurements described in this work, we have fabricated devices ranging in area from 0.04 to 100 $\mu m^2$, and we report measurements on 25 $\mu m^2$ structures. Photolithographic device patterning facilitates batch fabrication of many devices in parallel.

Lithographically patterned Pt counter electrodes serve as templates for an assembly of nanoparticle superlattices that form the active device material. Following the contact hole definition, we deposit drops of a monodisperse 6 nm diam $Fe_3O_4$ nanoparticle dispersion with controlled concentration and allow the liquid to dry slowly on the substrate.[15] We confirm the inverse spinel structure and spherical shape of the $Fe_3O_4$ nanoparticles using x-ray diffraction and high resolution TEM (HRTEM). Close examination of the nanoparticle array also reveals that the nanoparticles are randomly oriented single crystals (Fig. 1). Typical nanoparticle film thicknesses are roughly 200 nm (measured via profilometry), corresponding to ~20 particle layers. After the nanoparticle film formation, devices were annealed under high vacuum ($1 \times 10^{-7}$ torr) at 500 °C for 1 h, and coated *in situ* with a 300 nm Al gate. Annealing in high vacuum evaporates nano-

 

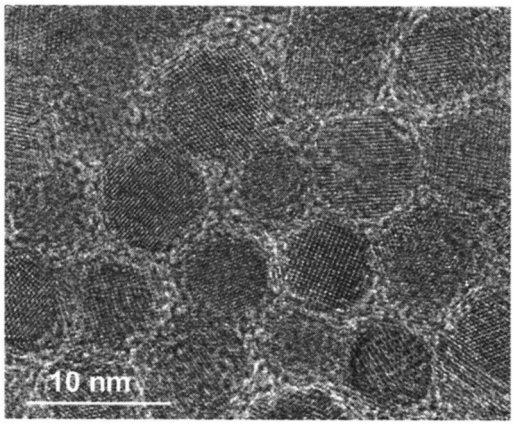


FIG. 1. HRTEM of an assembly of 6 nm diam $Fe_3O_4$ nanoparticles, showing randomly oriented crystal axes. The assembly was annealed at 500 °C for 1 h.

particle organic surfactants and also reduces interparticle distances, which is important in achieving significant electronic contact between particles. An elemental analysis reveals less than 1 at. % residual carbon in the nanoparticle layer, suggesting that high vacuum annealing eliminates most of the surfactants. Besides the removal of organic surfactants and the reduction of interparticle distances, we do not observe significant changes in the ordering of the nanoparticle assembly caused by the high temperature processing (Fig. 1).

We completed the devices by patterning the Al gate with a second lithography step and a wet-chemical etch. A schematic illustration of the device [Fig. 2(a)] shows a nanoparticle array sandwiched between the top Al gate and Pt counter electrode, with the current flowing perpendicularly from top to bottom. We note some advantages of this device geometry that (1) the gap between gate and counter electrodes is readily controlled by the number of particle layers deposited, and (2) the device conductance is increased due to many parallel current channels, each involving only small numbers of nanoparticles in a series.

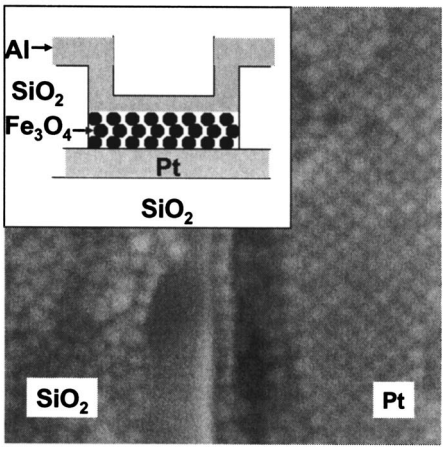


FIG. 2. SEM image of a device section, shown after nanoparticle deposition and annealing. Regions of nanoparticles assembled on the $SiO_2$ isolation layer and the Pt counter electrode are shown. Inset: Schematic illustration of a multilayer nanoparticle device.

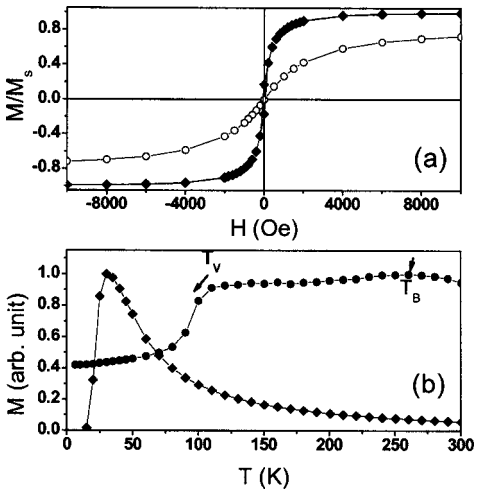


FIG. 3. (a) Magnetization versus applied magnetic field for a 6 nm $Fe_3O_4$ nanoparticle assembly measured at 300 K (circle) and 10 K (diamond); and (b) Zero-field-cooled magnetization curves for a 6 nm (diamond) and 12 nm (circle) $Fe_3O_4$ nanoparticle assembly.

By confining nanoparticles within the contact holes defining the device area, we form highly ordered superlattice arrays with a typical domain size on the order of 1 $\mu$m [Fig. 2(b)]. The right side of the scanning electron microscope image shows a portion of the patterned contact hole area, where particles self-assemble into a highly ordered array. Outside the device active area (left side of the image), the particles are more randomly distributed.

6 nm diam $Fe_3O_4$ nanoparticles are superparamagnetic at room temperature and become ferromagnetic upon cooling to low temperature, as evidenced in magnetization hysteresis loops [Fig. 3(a)]. At 10 K the nanoparticle coercivity is less than 200 Oe. From zero-field-cooled (ZFC) magnetization measurements [Fig. 3(b)], we determine the magnetic blocking temperature ($T_B$) of 40 K for this size nanoparticles. The ZFC curve of 12 nm particles is also plotted for comparison. Besides an enhanced superparamagnetic blocking temperature as evidenced by a peak at 260 K, a sharp drop in magnetization as the temperature is decreased to just below 110 K is also observed. This is an indication of the characteristic Verwey transition of magnetite, where an increase in magnetocrystalline anisotropy accompanying a distortion in the crystal structure leads to the reduction of magnetization as the sample is cooled through the transition point. This sharp drop in magnetization is not observed in 6 nm particles because their blocking temperature of 40 K is below the Verwey transition temperature. The nanoparticle magnetization at room temperature is well described by Langevin's equation, because of magnetite's small magnetocrystalline anisotropy due to its cubic spinel structure. The nanoparticle magnetization reaches 90% saturation at an applied field of 15 kOe.

Device current-voltage characteristics (I-V) are linear at room temperature with a resistivity of 5 $\Omega$ cm. The resistivity increases monotonically with decreasing temperature, reaching $\sim 3 \times 10^7$ $\Omega$ cm at 60 K. [Fig. 4(a)]. For $T$ below 160 K, the I-V characteristics become increasingly nonlinear, and below 40 K the devices are completely insulating.

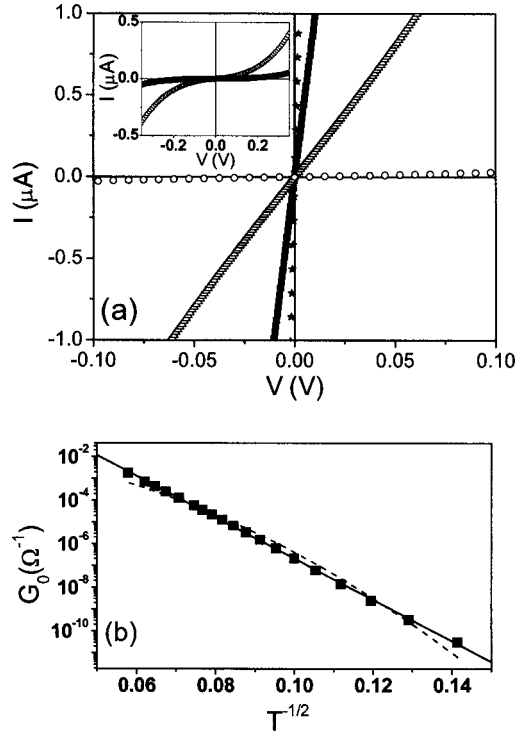


FIG. 4. (a) Device current versus voltage ($H=0$ Oe) curves measured at 300 K (star), 200 K (square), 160 K (triangle), and 100 K (circle). Inset: current versus voltage ($H=0$ Oe) curves measured at 100 K (circle) and 80 K (diamond); the curves show nonlinearity between the voltage range −0.4 V–0.4V. (b) Temperature dependence of zero-bias-voltage conductance ($G_0$), for a 25 $\mu m^2$ area device. Experimental data (square), best fit to $T^{-1/2}$ (solid line), best fit to $T^{-1}$ (dashed line); $G_0$ is plotted in a logarithmic scale.

The temperature dependence of device conductivity elucidates mechanisms of charge transport through the magnetite nanoparticle array. We expect electronic conduction energy barriers in our devices due to the nanocrystalline nature of the active material. Electronic transport through the device occurs by tunneling between nanoparticles, a process involving electrostatic charging.[13] Tunneling conductance of this type follows a $T^{-1/2}$ dependence (for a distribution of energy barriers).[16] In our devices, the zero-bias conductance ($G_0=dI/dV|_{V=0}$) varies with temperature as $T^{-1/2}$ [Fig. 4(b)], with our data best described by the relation $\ln(G_0)/\sqrt{T}=217\ \Omega^{-1}\ K^{-1/2}$. [For comparison, Fig. 4(b) also shows the best fit to a $T^{-1}$ relation, which would suggest hopping of the localized electrons within different lattice sites in the magnetite nanoparticle.[17]] Although our nanoparticles are monodisperse with $\delta d/d<5\%$, considering the large number of particles ($>10^6$) involved in the charge transport, we may expect a tunneling barrier distribution.

This observation implies that interparticle tunneling is the rate-limiting step in electronic transport through these materials, and that electrostatic charging effects dominate the effects of hopping barriers within individual magnetite particles.

We can estimate the electrostatic charging energy in the magnetite films using the relationship derived for the conductance of granular films:[16]

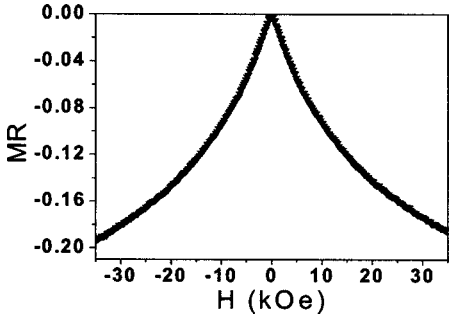


FIG. 5. $MR \equiv |\Delta R|/R(H=0)$ as a function of the applied field measured at a constant current of 1 nA and temperature of 100 K.

$$G_0 \propto \exp\left[-\sqrt{\frac{8\chi d E_c}{k_B T}}\right], \tag{1}$$

where $d$ is the interparticle spacing, $E_c=e^2/2C_\Sigma$ is the electrostatic activation energy for charging the array (with $C_\Sigma$ the average capacitance of a nanoparticle to its surroundings), $k_B$ is the Boltzmann constant, and $\chi=\sqrt{2m\phi/\hbar^2}\approx 10\ nm^{-1}$ ($\phi$ is the tunneling barrier height). Substituting values for our experimental system ($d\sim 1$ nm), we find $E_c\sim 50$ meV. This energy barrier is larger than the hopping activation energy measured in continuous $Fe_3O_4$ thin films (~20–40 meV).[17]

Magnetite nanoparticle devices display negative MR (i.e., device conductance increases with applied magnetic field, $H$), reaching a value as high as 35% (for $H=35$ kOe and $V_b=0$, where $V_b$ is the bias voltage) at T=60 K. Device MR decreases with increasing $T$ at a rate of roughly −0.1% per kelvin, with 12% remaining at 300 K. Typical magnetite thin films and heterostructures show a stronger temperature de-

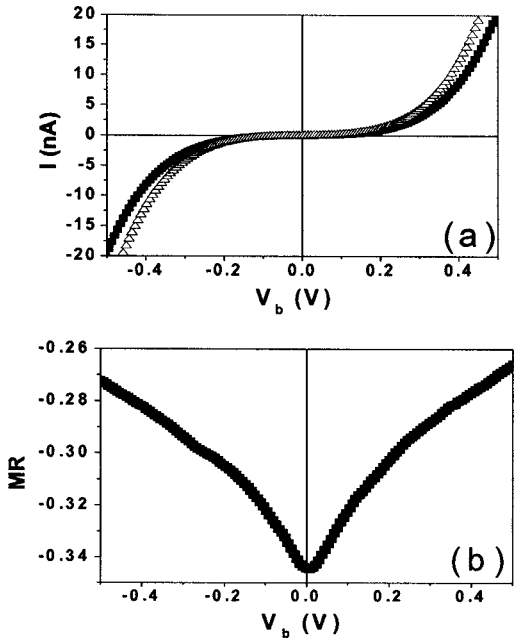


FIG. 6. (a) Current versus voltage measured at $H=0$ Oe (square) and $H=35$ kOe (triangle) and (b) $MR$ (obtained from I-V curves) as a function of the bias voltage ($V_b$) for a 25 $\mu m^2$ area device. Both (a) and (b) are measured at 80 K.

pendence, retaining a MR of only a few percent at room temperature.[18,19] $H$ aligns the electronic spins of adjacent nanoparticles, thereby increasing the tunneling probability (and conductance) for electrons moving through the array, leading to negative MR. Although the highest $H$ of 35 kOe is enough to saturate the nanoparticle magnetization [Fig. 3(a)], the device MR remains unsaturated (Fig. 5). Spin canting at the nanoparticle surfaces[20] may account for the difference in measured saturation field in magnetization ($\sim$10 kOe) and magnetoresistance ($>$35 kOe), as we expect surface electronic states to dominate electron transport characteristics while playing a lesser role in total particle magnetization.

The magnitude of MR in our devices is consistent with a half-metallic nature of the $Fe_3O_4$ nanoparticle material. In a granular material with randomly oriented magnetic easy axis, the MR is given by[21]

$$MR \equiv \frac{P^2}{1+P^2}, \tag{2}$$

where $P$ is the electronic spin polarization of the material. Substitution of the measured MR $\sim$35% into (2) yields P$>$73% in the $Fe_3O_4$ nanoparticles.

The MR of nanoparticle array devices is robust against degradations caused by the applied bias voltage $V_b$. Figure 6(a) shows I-V curves measured at 80 K, where the square and triangle points represent 0 field and 35 kOe data, respectively. Sizable differences in conductance can be observed. When $MR \equiv |\Delta R|/R(H=0)$ is plotted as a function of $V_b$, a monotonic decrease in MR with increasing $V_b$ is observed. MR shrinks by approximately $(35-27)/35=23\%$ as $V_b$ increases from 0 to 500 mV [Fig. 6(b)]. For a device comprised of $\sim$20 nanoparticle layers, $V_b=500$ mV corresponds to an effective nanoparticle temperature of $(k_B T_{eff} \sim 500\ \text{mV}/20 = 25\ \text{meV} = 300\ \text{K}$. We note that the effect of $V_b$ on MR is much weaker than that of the temperature; as at $T=300$ K we find that MR is only 12% in our devices. The different effects of $V_b$ and $T$ on MR can be traced to having many magnetic interfaces in conductance paths of different lengths through our devices. Thin film magnetic junction devices often show a steep reduction in MR with increasing $V_b$,[22] an effect that is detrimental to applications. The effect of $V_b$ on MR in nanoparticle devices is weaker when compared with typical high quality junction devices.[22] For example, the voltage at which MR reaches 50% of the maximum value is 0.3 V in the devices of Ref. 22, while a $V_b=0.3$ V only reduces the MR of our devices by 16% [Fig. 6(b)]. This result is consistent with theoretical calculations of a reduced $V_b$ dependence of MR in multiple-tunnel-junction devices.[12]

We have demonstrated a method for fabricating nanoparticle multilayer devices that combines advantages of conventional microfabrication with self-assembly. The versatility of this technique has enabled our study of electronic conduction in magnetite nanoparticle arrays. The electronic signature of these materials is dominated by a high barrier (50 meV) for conduction between nanoparticles, as well as a high degree of electronic spin polarization (73%).

[1] P. Coehoorn, in *Magnetic Multilayers and Giant Magnetoresistance: Fundamentals and Industrial Applications*, edited by U. Hartmann (Springer, Berlin, 2000), p. 65.
[2] P. M. Levy and S Zhang, Curr. Opin. Solid State Mater. Sci. **4**, 223 (1999).
[3] R. A. de Groot, F. M. Mueller, P. G. van Engen, and K. H. J. Buschow, Phys. Rev. Lett. **50**, 2024 (1983).
[4] V. A. M. Brabers, in *Handbook of Magnetic Materials*, edited by K. H. J. Buschow (North-Holland, Amsterdam, 1998), Vol. 8, p. 189.
[5] V. V. Gridin, G. R. Hearne, and J. M. Honig, Phys. Rev. B **53**, 15518 (1996).
[6] J. M. D Coey, A. E. Berkowitz, L I. Balcells, F. F. Putris, and F. T. Parker, Appl. Phys. Lett. **72**, 734 (1998).
[7] G. Q. Gong, A. Gupta, G. Xiao, W. Qian, and V. P. Dravid, Phys. Rev. B **56**, 5096 (1997).
[8] K. Liu, L. Zhao, P. Klavins, F. E. Osterloh, and H. Hiramatsu, J. Appl. Phys. **93**, 7951 (2003).
[9] P. A. Dowben and R. Skomski, J. Appl. Phys. **95**, 7453 (2004).
[10] E. Y. Tsymbal, O. N. Mryasov, and P. R. LeClair, J. Phys.: Condens. Matter **15**, R109 (2003).
[11] K. Yakushiji, S. Mitani, K. Takanashi, S. Takanashi, S. Maekawa, H. Imamura, and H. Fujimori, Appl. Phys. Lett. **78**, 515 (2001).
[12] A. Vedyayev, N. Ryzhanova, R. Vlutters, B. Dieny, and N. Strelkov, J. Phys.: Condens. Matter **12**, 1797 (2000).
[13] C. T. Black, C. B. Murray, R. L. Sandstrom, and Shouheng Sun, Science **290**, 1131 (2000).
[14] P. Poddar, T. Fried, and G. Markovich, Phys. Rev. B **65**, 172405 (2002).
[15] 6 nm $Fe_3O_4$ nanoparticles were prepared by a high temperature solution phase reduction of $Fe(acac)_3$ using polyol. The synthetic details are published in Shouheng Sun and Hao Zeng, J. Am. Chem. Soc. **124**, 8204 (2002).
[16] P. Sheng, B. Abeles, and Y. Arie, Phys. Rev. Lett. **31**, 44 (1973).
[17] B. Raquet, J. M. D. Coey, S. Wirth, and S. Von Molnar, Phys. Rev. B **59**, 12435 (1999).
[18] G. Hu and Y. Suzuki, Phys. Rev. Lett. **89**, 276601 (2002).
[19] S. B. Ogale, K. Ghosh, R. P. Sharma, R. L. Greene, R. Ramesh, and T. Venkatesan, Phys. Rev. B **57**, 7823 (1998).
[20] M. P. Morales, S. Veintemillas-Verdaguer, M. I. Montero, C. J. Serna, A. Roig, L. Casas, B. Martinez, and F. Sandiumenge, Chem. Mater. **11**, 3058 (1999); B. Stahl, J. Ellrich, R. Theissmann, M. Ghafari, S. Bhattacharya, H. Hahn, N. S. Gajbhiye, D. Kramer, R. N. Viswanath, J. Weissmuller, and H. Gleiter, Phys. Rev. B **67**, 014422 (2003).
[21] J. Inoue and S. Maekawa, Phys. Rev. B **53**, 011927 (1996).
[22] J. S. Moodera, J. Nowak, and P. van de Verdonk, Phys. Rev. Lett. **80**, 2941 (1998).